

Marquette University

e-Publications@Marquette

---

Electrical and Computer Engineering Faculty  
Research and Publications

Electrical and Computer Engineering,  
Department of

---

6-2011

## Multispectral Classification With Bias-Tunable Quantum Dots-in-a-Well Focal Plane Arrays

Biliana S. Paskaleva


Woo-Yong Jang

Yagya D. Sharma

Sanjay Krishna

Majeed M. Hayat

Follow this and additional works at: [https://epublications.marquette.edu/electric\\_fac](https://epublications.marquette.edu/electric_fac)

 Part of the [Computer Engineering Commons](#), and the [Electrical and Computer Engineering Commons](#)

---

Marquette University

**e-Publications@Marquette**

***Electrical and Computer Engineering Faculty Research and Publications/College of Engineering***

***This paper is NOT THE PUBLISHED VERSION; but the author's final, peer-reviewed manuscript.*** The published version may be accessed by following the link in the citation below.

*IEEE Sensors Journal*, Vol. 11, No. 6 (June 2011): 1342-1351. [DOI](#). This article is © Institute of Electrical and Electronic Engineers (IEEE) and permission has been granted for this version to appear in [e-Publications@Marquette](#). Institute of Electrical and Electronic Engineers (IEEE) does not grant permission for this article to be further copied/distributed or hosted elsewhere without the express permission from Institute of Electrical and Electronic Engineers (IEEE).

# Multispectral Classification With Bias-Tunable Quantum Dots-in-a-Well Focal Plane Arrays

Biliana S. Paskaleva

Sandia National Laboratories, Albuquerque, NM

Woo-Yong Jang

Center for High Technology Materials and the Department of Electrical and Computer Engineering, University of New Mexico, Albuquerque, NM

Yagya D. Sharma

Center for High Technology Materials and the Department of Electrical and Computer Engineering, University of New Mexico, Albuquerque, NM

Sanjay Krishna

Center for High Technology Materials and the Department of Electrical and Computer Engineering, University of New Mexico, Albuquerque, NM

Majeed M. Hayat

Center for High Technology Materials and the Department of Electrical and Computer Engineering, 1 University of New Mexico, Albuquerque, NM

## Abstract:

Mid-wave and long-wave infrared (IR) quantum-dots-in-a-well (DWELL) focal plane arrays (FPAs) are promising technology for multispectral (MS) imaging and sensing. The DWELL structure design provides the detector with a unique property that allows the spectral response of the detector to be continuously, albeit coarsely, tuned with the applied bias. In this paper, a MS classification capability of the DWELL FPA is demonstrated. The approach is based upon: 1) imaging an object repeatedly using a sequence of bias voltages in the tuning range of the FPA and then 2) applying a classification algorithm to the totality of readouts, over multiple biases, at each pixel to identify the “class” of the material. The approach is validated for two classification problems: separation among different combinations of three IR filters and discrimination between rocks. This work is the first demonstration of the MS classification capability of the DWELL FPA.

## SECTION I. Introduction

Typical infrared (IR) multispectral (MS) and hyperspectral (HS) systems are usually implemented by deploying multiple detectors, each sensing at a specific range of wavelengths. Another alternative is to use a single broadband detector combined with a dispersive optical system, such as a bank of IR optical filters, each tuned to a specific wavelength band. In either case, the sensor represents a highly complex optomechanical system that requires precision alignment and calibration. Once the calibration is completed and the sensor is deployed, the sensor's functionality cannot be easily modified. As a result, the sensor cannot be easily adapted to take advantage of specific sensing situations. In the absence of an agile software/hardware architecture, one is typically forced to acquire all available imagery data before its relevance becomes clear. This leads to the acquisition of maximum and often massive amounts of data that has to be stored for subsequent processing in applications such as classification, abundance estimation, image segmentation and analysis, etc. Besides the large storage demands, the analysis of this MS and HS imagery requires powerful hardware systems and efficient processing algorithms.

The inflexibility of the functionality of most present-day MS/HS sensors to adapt to specific applications has prompted the development of a new modality for MS and HS sensing, providing greater flexibility in terms of compressive data acquisition and offering reduced complexity and cost. Spectrally adaptive sensing methods include those that are based on microelectromechanical systems (MEMS) [1] and acousto-optic tunable filters (AOTFs) [2]. However, a new emerging technology for adaptable and compressive sensing is the quantum dots-in-a-well (DWELL)-based IR focal plane array (FPA) [3]–[4][5]. Owing to the quantum-confined Stark effect (QCSE) [6], [7], the DWELL sensor exhibits a unique feature that enables continuous spectral tuning in the mid-wave infrared (MWIR) and long-wave infrared (LWIR) spectral regions by means of changing the applied bias voltage. Such tunable sensors provide greater optical simplicity because their spectral response is controlled electrically rather than optically or mechanically.

Fig. 1(a) shows the spectral responses of a single-pixel DWELL device. As seen in the figure, the central wavelength and the shape of the detector's responsivity change continuously with the applied bias voltage. Furthermore, the spectral diversity offered by the DWELL can be further enhanced by design via optimizing the well width and the asymmetric band structure. As a result, in the context of MS and HS sensing, a single DWELL detector can be exploited as a MS IR sensor; the photocurrents measured at different operational biases can be viewed as outputs of different spectrally broad and overlapping bands. Clearly, this capability is an excellent fit to compressive sensing once the sensor is combined with algorithms and reconfigurable readout integrated circuits (ROICs).

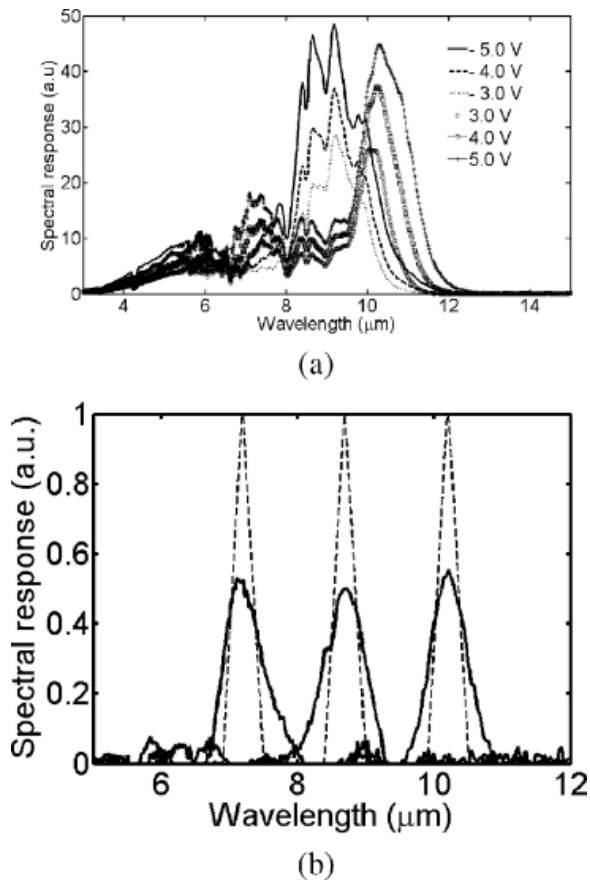


Fig. 1. (a) Spectral responses of a DWELL detector as a function of the applied bias which demonstrate the tuning capability. (b) Series of synthesized filters (solid lines) in the projection stage of algorithmic spectrometer with full width half maximum (FWHM) of  $0.3 \mu\text{m}$ .

The flexibility offered by the DWELL FPA is not without a price, however. For instance, the DWELL's spectral response is relatively broad ( $\approx 1\text{--}2\mu\text{m}$ ). As a result, the spectral bands corresponding to different bias voltages exhibit significant overlap. Another complication is the bias-dependence of the noise (dark current) in the photocurrents. In our previous works, we targeted addressing both of these challenges. In particular, the DWELL-based algorithmic spectrometer (DAS), proposed in [8] and demonstrated in [9] and [10], banks on using linear superposition of bias-tunable bands of the individual DWELL detector to minimize the effect of high correlation in the DWELL's bands in the presence of noise in achieving target spectrum reconstruction. Fig. 1(b) shows series of synthesized filters (solid lines) which approximate ideal tuning filters (dashed lines) in the projection stage of the DAS. The full width half maximum (FWHM) of the synthesized filters is  $0.3 \mu\text{m}$ .

Another example is the canonical correlation feature selection (CCFS) algorithm, reported in [11] and [12]. This algorithm addresses the problem of linear superposition of bias-tunable DWELL bands to perform spectral feature selection (for material classification) based on spectral matched filtering. Our previous work [11] also includes successful demonstration of MS classification of the DWELL detector, at a single-pixel level, in terms of rock-type classification. The study was conducted using laboratory spectral data for the rock types and spectral responsivities measurements of the DWELL detector.

In this paper, we demonstrate for the first time MS classification using imagery obtained from the DWELL FPA. In our setting, multiple DWELL-FPA images are taken at different bias voltages. As such, the sequence of all images can be viewed as a MS imagery. We performed two studies. In the first study, we compare the classification error among different materials for two general classification problems using few combinations of bias voltages.

The first classification problem, termed filter classification problem, is that of classifying combinations of MWIR and LWIR optical filters with different bandwidths and center wavelengths. The second classification problem, termed rock classification problem, focuses on classification between pairs of rocks drawn from a set of three distinct rock types: granite, hornfels, and limestone.

The second study is a separability analysis and optimal bias selection for classification. The separability analysis focuses on investigation of the separation between pairs of materials as a function of the DWELL's bias voltage. For the granite-limestone and granite-hornfels classification problems, we carry out exhaustive search over all possible combinations of the bias voltages in the context of optimal bias selection based on minimization of the classification error.

The organization of this paper is as follows. In Section II, we briefly describe the development and the operation principle of the DWELL FPA, followed by the description of the bias-dependent spectral tunability capability of the DWELL FPA. Section III describes the MS classification approach for the two classification problems described above. In Section IV, the MS classification results are discussed. The separability and classification analysis for optimal bias selection are also presented and discussed in Section IV. Our conclusions are presented in Section V.

## SECTION II. The DWELL Focal Plane Array

In this section, we briefly describe the operation principle, characterization and bias-dependent spectral tunability of the DWELL FPA.

### A. Operation Principle and Spectral Characterization of the DWELL FPA

The DWELL photodetector, pioneered by Krishna [13], is a hybrid version of quantum dot (QD) and quantum well (QW) photodetectors. The DWELL photodetector reported in [9] has already been shown to exhibit bias tunability in the range of MWIR (3–5  $\mu\text{m}$ ) to the LWIR (8–12  $\mu\text{m}$ ) portions of the spectrum. In general, the MWIR response is driven by a bound-to-continuum transition, while the LWIR is driven by the bound state in the dot-to-a-bound state in the well transition, as shown in Fig. 2. In addition, the asymmetry of the electronic potential controlled by the shape of the dot and the different thicknesses of QW above and below the dot, results in variation of the local potential as a function of the applied bias. As a result, by adjusting the applied bias voltage on the device, spectral shift (called also “redshift”) and overlaps are obtained, particularly in LWIR (8–12  $\mu\text{m}$ ) region.

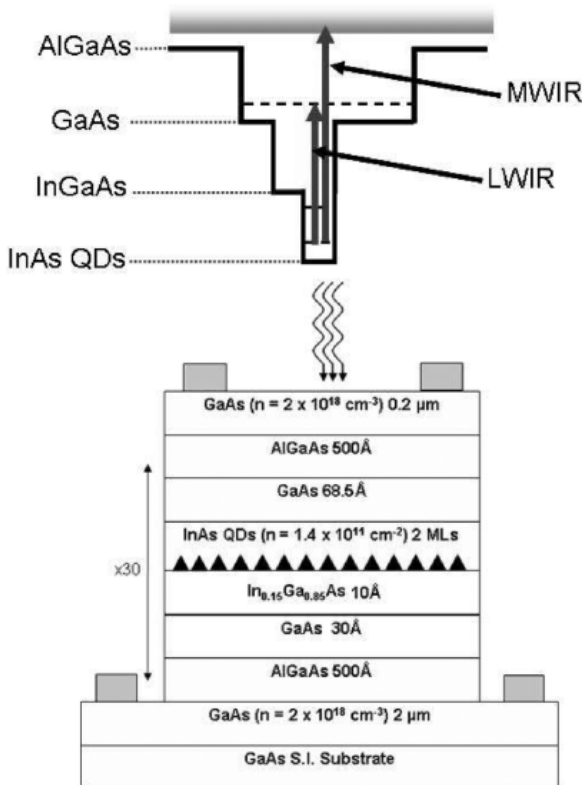


Fig. 2. Top: schematic of the energy transition levels in the conduction band of DWELL. Bottom: growth schematic of single-pixel DWELL (adapted from [9].).

The spectral responses of the single-pixel DWELL shown in Fig. 3 demonstrate bias-dependent spectral tunability for various device operating temperatures. The details of the device characterization had been reported in [9]. The DWELL has been fabricated into a 320 by 256 detector array format and is used for this study. The fabrication process is described in great detail in [14] and [15]. The DWELL FPA responses have been characterized by using CamIRa demonstration system.<sup>1</sup> Recently, an optimized DWELL FPA was reported in [14] demonstrating an increase in the operating temperature (up to 80 K) and smaller noise equivalent difference in temperature (min. NEDT<sup>2</sup> around 78 mK). The higher operating temperature has been achieved by a strain reduction and an increased number of stacks in the active region, improving the responsivity and the absorption quantum efficiency.

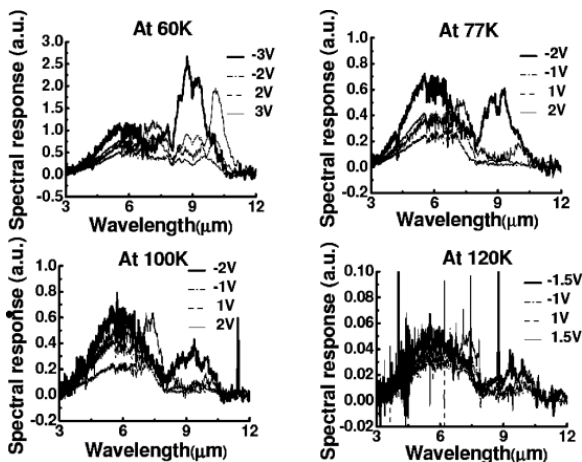


Fig. 3. Bias-tunable spectral responses of the single-pixel DWELL photodetector for various operating temperatures (adapted from [12]).

## B. Bias Tunability of the DWELL FPA

DWELL FPA imagery shown in Fig. 4(a)–(d) are used to demonstrate the DWELL FPA bias tunability. For all imagery, the operating temperature of the DWELL FPA was set to 60 K and the integration (exposure) time was 11.5 ms. The images shown in columns one, three and five in Fig. 4(a)–(d) are taken at 0.3, 0.7, and 1.2 V, respectively. Normalized images at 0.3, 0.7, and 1.2 V are shown in columns two, four, and six, respectively, in Fig. 4(a)–(d). The DWELL FPA data is normalized at each pixel by the approximate area of the multibias pixel response in order to eliminate the intensity effect in the calculations. More details about the normalization are given in Section III.

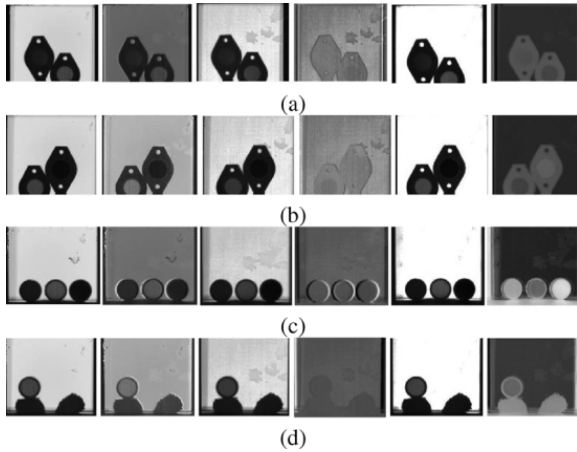


Fig. 4. Columns one, three, and five, a-d show DWELL FPA raw imagery acquired at 0.3, 0.7, and 1.2 V, respectively. Columns two, four, and six, a-d, show the normalized imagery at 0.3, 0.7, and 1.2 V, respectively. For more details on the normalization, please refer to Section III. Objects in scene; scene in row (a): filters MW1 (left) and MW2 (right); scene in row (b): filters MW2 (left) and LW3 (right); scene in row (c): filters MW1 (left), MW2 (center) and LW3 (right); scene in row (d): filter MW2 (top), limestone (left) and granite (right).

Fig. 4(a)–(c) contains images of different configurations of three IR optical filters, manufactured by Northumbria Optical Coatings, Ltd. The spectral responses of the filters are shown in Fig. 5 (left). The first scene, shown in Fig. 4(a) includes two IR filters: filter at 3–4  $\mu\text{m}$  termed MW1, filter at 4–5  $\mu\text{m}$  termed MW2, metal filter holders, and a blackbody background at 150  $^{\circ}\text{C}$ . A 150  $^{\circ}\text{C}$  temperature was used since such a high-temperature blackbody offered a good transmittance for objects in a scene. The blackbody is manufactured by MIKRON company (model M315) providing a temperature between ambient 5  $^{\circ}\text{C}$  and 350  $^{\circ}\text{C}$ , a control to within 0.2  $^{\circ}\text{C}$  and an emissivity of +0.99.

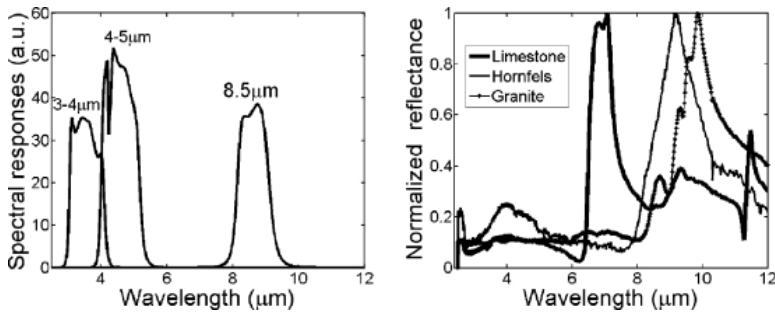


Fig. 5. Left: spectral responses of the three IR optical filters: MW1, MW2, and LW3. Right: normalized (by the peak value) reflectance spectra of granite, hornfels, and limestone.

The second scene shown in Fig. 4(b) consists of two filters: MW<sub>2</sub> and filter at 8.5 μm termed LW<sub>3</sub>, the same metal filter holders and the uniform background at the same temperature. The third scene in Fig. 4(c) consists of all three filters MW<sub>1</sub>, MW<sub>2</sub>, and LW<sub>3</sub> and the background. The scene in Fig. 4(d) includes two rocks: granite and limestone, and the MW<sub>2</sub> filter. Granite is a common and widely occurring type of intrusive, felsic igneous rock. Granites usually have a medium to coarse grained texture. Limestone is a sedimentary rock composed largely of the minerals calcite and aragonite, which are different crystal forms of calcium carbonate. Hornfels is a fine-grained nonfoliated metamorphic rock with no specific composition. It is produced by contact metamorphism. Normalized reflectance measurements of granite, limestone, and hornfels using a broadband single-pixel HgCdTe device cooled to 77 K are shown in Fig. 5 (right).

Fig. 6, left and right, shows plots of the normalized DWELL FPA multibias responses for every object from the scenes in Fig. 4(a) and (d), respectively. The multibias response for every object is averaged over spatially uniform regions that are visually associated with that object. From the plots in Fig. 6 (left), we can observe that at bias voltages 0.7 and 0.8 V the responses of the DWELL FPA for all objects exhibit significant overlap. Higher separation between all objects for this problem is observed in the bias range of 0.3–0.6 V and in the range of 1.0–1.2 V.

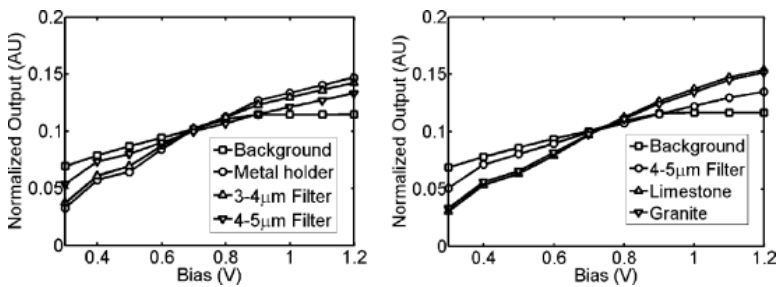


Fig. 6. Left: normalized multibias FPA responses for background, metal holder, MW<sub>1</sub>, and MW<sub>2</sub> as a function of applied DWELL FPA bias. Right: normalized multibias FPA responses for background, MW<sub>2</sub>, limestone, and granite as a function of applied DWELL FPA bias.

The normalized multibias FPA responses for granite, limestone, background and filter comprising the scene in Fig. 4(d) overlap at bias voltages 0.7 and 0.8 V, as observed in Fig. 6 (right). The pairwise separability between the normalized multibias FPA responses for granite and limestone has the lowest value at 0.6 V. At 0.9 V, the normalized multibias FPA responses for the black-body background and the filter are very close to each other. The rest of the biases provide a good separability between the black-body background and the filter, and the black-body background and each one of the two rocks. The pairwise separability between the multibias responses for the two rocks, granite and limestone, is low across the entire bias range making this problem very challenging for MS classification.

Fig. 7, left and right, shows plots of the spectral ratios for pairs of sensed materials in as a function of the applied bias. Fig. 7 (left) shows the spectral ratios calculated for the pair of objects (filters, background and metal holder) from the scene in Fig. 4(b). The spectral ratios vary between 0.4 to almost 1.4 when the applied bias changes in the range from 0.3 to 1.2 V with a step of 0.1 V. Note that for bias voltages 0.7 and 0.8 V, the ratios between pair of objects are close to one, indicating low spectral separability between the materials at these particular biases.



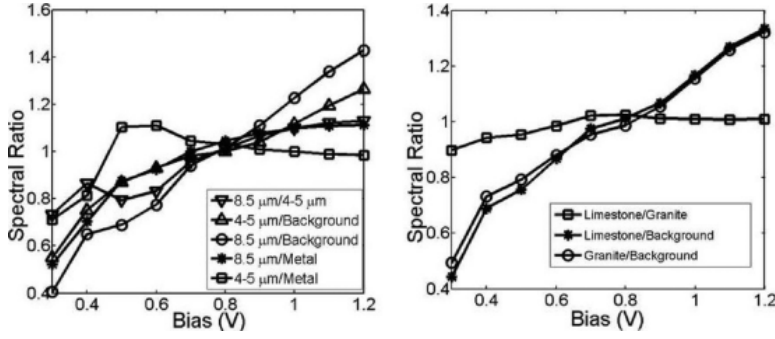


Fig. 7. Left: ratio of pixel values for various pairs of the objects MW2, LW3, metal holder, and the background as a function of applied DWELL FPA bias. Right: ratio of pixel values between objects granite and limestone, granite and background, and limestone and background as a function of applied DWELL FPA bias.

The fact that the ratio values change from one bias to another indicates that the DWELL FPA can sense different spectral contents of the targets observed in a scene simply by changing the applied bias. Note that for the conventional (nontunable) detector the spectral ratios would remain fixed as a function of the applied bias.

Fig. 7 (right) shows spectral ratio plots for two rocks: granite and limestone, and the background. As observed from the plots in Fig. 7 (right), the ratio between granite and limestone does not exhibit wide range as, for example, the granite-background ratio or limestone-background ratio. Note that for bias voltages 0.6, 0.7, and 0.8 V, the ratios between granite and limestone are close to one, indicating low spectral separability at these biases. The classification results presented in Section IV demonstrate that the spectral contrast captured by the bias-tunable DWELL FPA is sufficient to discriminate between the two types of rocks.

### SECTION III. Multispectral Classification Using Bias Tunable DWELL FPA

In this section, we provide a brief overview of the mathematical model for bias-tunable MS sensing and discuss the classification approach.

#### A. Bias-Tunable MS Sensing

Mathematically, the DWELL spectral bands can be viewed as a family of functions  $\{f_{v_i}(\lambda)\}$ , parameterized by the applied bias voltages  $v_i$  [11]. In what follows, we denote the spectrum of an object by  $p(\lambda)$ . For example,  $p(\lambda)$  may represent transmittance, bidirectional reflectance measurement or hemispherical reflectance data. The photocurrent for the  $i$ th band of the DWELL detector sensing an object with a given spectrum  $p(\lambda)$  can be written as

$$I_{v_i} = \int_{\lambda_{min}}^{\lambda_{max}} p(\lambda) f_{v_i}(\lambda) d\lambda + N_{v_i}. \quad (1)$$

Here,  $N_{v_i}$  denotes additive, scene-independent noise associated with the  $i$ th band, and the interval  $[\lambda_{min}, \lambda_{max}]$  represents the common spectral support for all bands and objects. Next, for a given set of applied bias voltages  $\{v_1, \dots, v_n\}$ , the output of the DWELL detector is a set of photocurrents at these bias voltages

$$\mathbf{I} = (I_{v_1}, \dots, I_{v_n}). \quad (2)$$

This set represents the multibias or MS signature of the object as “seen” by the DWELL detector.

Because the DWELL bands are wide and overlapping, the photocurrents in  $\mathbf{I}$  are highly correlated. The redundancy in the information content of the photocurrents can be reduced by a suitable postprocessing

algorithm, which, in turn, can be used to improve the efficiency of the classification process. Here, we shall use the CCFS [11] algorithm to replace the  $n$ -dimensional multibias signature in (2) by a single feature that is optimized with respect to a given class of objects.

For a given class of objects represented by a mean spectrum  $\bar{p}(\lambda)$ , the output from the CCFS algorithm is a single transformed feature  $\tilde{I} = \sum_{i=1}^n a_i I_{v_i}$ , which is a weighted linear combination of all features in (2). The weights  $a_i$  are optimized by the CCFS for every class of objects represented by their mean spectrum  $\bar{p}(\lambda)$ .

The transformed feature  $\tilde{I}$  can be viewed as the current generated by a “virtual” superposition band,  $\tilde{f} = \sum_{i=1}^n a_{v_i} f_{v_i}$ ; the optimal selection rule of the weights is derived rigorously in [11]. Consequently, the problem of determining the optimal current,  $\tilde{I}$ , for a given class representative or class mean spectrum  $\bar{p}(\lambda)$ , is equivalent to finding a superposition band  $\tilde{f}$  that provides the best approximation of  $\bar{p}(\lambda)$ .

Mathematically,  $\tilde{f}$  can be interpreted as an approximation of  $\bar{p}(\lambda)$  in the space spanned by  $\{f_{v_i}\}$ , which minimizes the distance and at the same time maximizes the signal-to-noise ratio [11].

## B. Classification Problems

The first classification problem considered in this paper is that of separating multiple combinations of MW and LW IR spectral filters with different bandwidths and center wavelengths. For this problem, we used the three scenes shown in Fig. 4(a)–(c). The second classification problem is to discriminate between pairs of rocks drawn from a set of three distinct rock types: granite, hornfels, and limestone. The scene configurations for this problem are shown in Figs. 4(d) and 9, left. The classes identified for both classification problems are summarized in Table I.

**Table I** Summary of Identified Classes for the Filters and Rock Classification Problems

Filter classification problem	Identified classes
Scene (a)	MW <sub>1</sub> , MW <sub>2</sub> filters, metal holder and background
Scene (b)	MW <sub>2</sub> , LW <sub>3</sub> filters, metal holder and background
Scene (c)	MW <sub>1</sub> , MW <sub>2</sub> and LW <sub>3</sub> filters and background
Rock classification problem	Identified classes
Scene (a)	MW <sub>2</sub> filter, limestone, granite and background
Scene (b)	granite, hornfels and background

Filter classification problem	Identified classes
Scene (a)	MW <sub>1</sub> , MW <sub>2</sub> , filters, metal holder and background
Scene (b)	MW <sub>2</sub> , LW <sub>3</sub> filters and metal holder and background
Scene (c)	MW <sub>1</sub> , MW <sub>2</sub> and LW <sub>3</sub> filters and background
Rock classification problem	Identified classes
Scene (a)	MW <sub>2</sub> filter, limestone, granite and background
Scene (b)	Granite, hornfels and background

Two types of normalization techniques are applied to the raw digital numbers (DNs) that are retrieved directly from the DWELL FPA. First, at each bias voltage, pixel's DN values are radiometrically corrected by a two-point nonuniformity correction (NUC) algorithm. The NUC compensates for the spatially nonuniform response of the

detectors within the FPA [16] and is an integrated part of the image acquisition process. The two-point NUC is performed using temperatures at 22 °C and 150 °C. The lower temperature of 22 °C corresponds to the lens-cap's room temperature, which was used to yield the lower-temperature uniform field.

Next, for every radiometrically corrected pixel and its replicas at each bias voltage, the pixel's value is normalized as follows:

$$\underline{I}(v_j) = \frac{I(v_j)}{\Delta v \sum_{i=1}^n I(v_i)} \quad (3)$$

where  $\Delta v$  is the voltage step size used to increment the DWELL FPA's bias. Equation (3) is equivalent to normalization by the area enclosed under the multibias response of each pixel in the DWELL FPA. The normalized multibias response of a pixel can then be written as

$$\underline{\mathbf{I}} = (\underline{I}(v_1), \dots, \underline{I}(v_n)). \quad (4)$$

This normalization minimizes the role of broadband emissivity in the discrimination process and emphasizes the spectral contrast. The normalized images at 0.3, 0.7, and 1.2 V for both classification problems are shown in columns two, four, and six in Fig. 4(a)–(d) and in Fig. 9 (left), respectively.

We perform a supervised classification comprising of training and testing steps for both classification problems. To determine representative multibias signatures for each class listed in Table I, we follow the same approach as used in [11]. Specifically, for each class we compute statistical mean and covariance matrix using spatially uniform regions that are visually associated with that class. Subsequently, Euclidean- and Mahalanobis-distance classifiers are trained by the classes' mean multibias signatures and the covariance matrices [17].

At the testing step, the trained classifiers are used to classify the objects in Table I from a set of testing scenes. These scenes capture the same images as the training scenes but were acquired at different times. As a result, the testing scenes carry inherent variability in the data due to the difference in the measurement conditions from day-to-day and the presence of ambient and system noise. The testing images are normalized in the same fashion as the training images. The size of training and testing data set for the filter and rock classification problems are listed in Table II.

**Table II** Number of Pixels Used in the Training and Testing Data Sets for the Filter and Rock Classification Problems

Filter classification problem	Number of pixels in training /testing sets
Scene (a)	MW <sub>1</sub> : 140/235, MW <sub>2</sub> : 140/235, metal holder: 66/161, background:300/300
Scene (b)	MW <sub>2</sub> : 154/330, LW <sub>3</sub> : 108/320, metal holder: 126/260, background: 352/340
Scene (c)	MW <sub>1</sub> : 400/280, MW <sub>2</sub> : 400/280, LW <sub>3</sub> : 400/280, background: 336/350
Rock classification problem	Number of pixels in training /testing sets
Scene (a)	granite: 340/420, limestone: 360/450, MW <sub>2</sub> : 360/300, background: 336/400
Scene (b)	granite: 224/526, hornfels: 308/870, background: 300/300

Filter classification problem	Number of pixels in training/testing sets
Scene (a)	MW <sub>1</sub> : 140/235, MW <sub>2</sub> : 140/235, metal holder: 66/161, background: 300/300
Scene (b)	MW <sub>2</sub> : 154/330, LW <sub>3</sub> : 108/320, metal holder: 126-260, background: 352/340
Scene (c)	MW <sub>1</sub> : 400/280, MW <sub>2</sub> : 400/280, LW <sub>3</sub> : 400/280, background: 336/350
Rock classification problem	Number of pixels in training/testing sets

Scene (a)	Granite: 340/420, limestone: 360/450, MW <sub>2</sub> : 360/300, background: 336/400
Scene (b)	Granite: 224/526, hornfels: 308/870, background 300/000

## SECTION IV. Discussion of the Results

### A. Classification Results

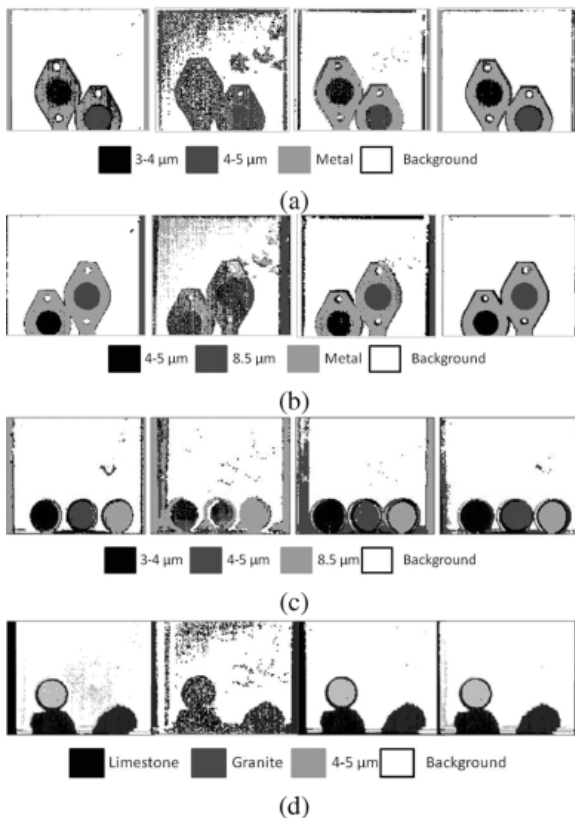


Fig. 8. Thematic maps, from left to right: bias at 0.3 V used, bias at 0.7 V used, combination of biases at 0.6 and 0.7 V used, and all biases in the range of 0.3–1.2 V used; (a) MW<sub>1</sub> and MW<sub>2</sub>; (b) MW<sub>2</sub> and LW<sub>3</sub>; (c) MW<sub>1</sub>, MW<sub>2</sub> and LW<sub>3</sub>; (d) thematic maps for MW<sub>2</sub>, limestone and granite, left to right: bias at 0.4 V used; bias at 0.7 V used; biases at 0.3 and 0.4 V used, all biases in the range of 0.3 to 1.2 V used.

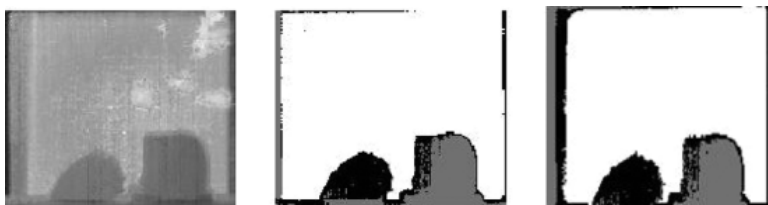


Fig. 9. Left: normalized image at 0.6 V where the rock on the left is granite and the rock on the right is hornfels (shown also in [18]); middle: thematic maps for granite-hornfels classification problem when all biases in the range of 0.3–1.2 V used (shown also in [18]); right: thematic maps for granite-hornfels classification problem when two superposition bands derived by CCFS are used.

The thematic maps for the filter and rock classification problems using Euclidean-distance classifier are presented in Figs. 8(a)–(d) and 9, respectively. These maps show the distribution of the derived classes over the spatial area captured by the DWELL FPA. Each map defines a partitioning of the area into sets, each including the points with identical class labels. In order to investigate the effect of the bias selection on the classification accuracy, the classification is performed for multiple combinations of biases.

The results for the filter classification problem, specified in Table I, are shown in Fig. 8(a)–(c), and Table III shows the calculated classification errors per various class. The thematic maps in Fig. 8(a)–(c) are obtained using four different sets of bias voltages: (i) one bias at 0.3 V; (ii) one bias at 0.7 V; (iii) two biases at 0.6 and 0.7 V; and (iv) all biases in the range of 0.3–1.2 V.

**Table III** Classification Errors in the Filter Classification Problem Using Euclidean-Distance Classifier

Problem 1 (a)	Bias (V)	MW <sub>1</sub> Error [%]	MW <sub>2</sub> Error [%]	Metal Error [%]
	0.3	2	0.4	32
	0.7	63	4	70
	0.6, 0.7	15	0.8	0
	0.3 – 1.2	0.8	0	0
Problem 1 (b)	Bias (V)	MW <sub>2</sub> Error [%]	LW <sub>3</sub> Error [%]	Metal Error [%]
	0.3	0	0	5
	0.7	64	44	23
	0.6, 0.7	0.5	0	7
	0.3 – 1.2	0	0	5
Problem 1 (c)	Bias (V)	MW <sub>1</sub> Error [%]	MW <sub>2</sub> Error [%]	LW <sub>3</sub> Error [%]
	0.3	0	2.5	4
	0.7	42.75	58.5	4.5
	0.6, 0.7	1	2.7	1
	0.3 – 1.2	1.7	1.7	0

Problem 1 (a)	Bias (V)	MW <sub>1</sub> Error [%]	MW <sub>2</sub> Error [%]	Metal Error [%]
	0.3	2	0.4	32
	0.7	63	4	70
	0.6, 0.7	15	.08	0
	0.3 -1.2	0.8	0	0
Problem 1 (b)	Bias (V)	MW <sub>2</sub> Error [%]	LW <sub>3</sub> Error [%]	Metal Error [%]
	0.3	0	0	5
	0.7	64	44	23
	0.6, 0.7	0.5	0	7
	0.3-1.2	0	0	5
Problem 1 (c)	Bias (V)	MW <sub>1</sub> Error [%]	MW <sub>2</sub> Error [%]	LW <sub>3</sub> Error [%]
	0.3	0	2.5	4
	0.7	42.75	58.5	4.5
	0.6, 0.7	1	2.7	1
	0.3-1.2	1.7	1.7	0

**Table IV** Classification Errors for the Rock Classification Problem Using Euclidean-Distance Classifier and Two CCFS Bands for the Granite-Hornfels Problem

Problem 2 (a)	Bias (V)	MW <sub>2</sub> Error [%]	Limestone Error [%]	Granite Error [%]
	0.4	2.076	29.81	1.91
	0.7	62.62	47.26	17.94
	0.3, 0.4	0.34	12.77	3.82
	0.3 – 1.2	0.34	17.84	1.43
Problem 2 (b)	Bias (V)	Granite Error [%]	Hornfels Error [%]	–
	0.3	55	46	–
	1.1	0	20	–
	0.6, 0.7	5	27	–
	0.3 – 1.2	1	17	–
	CCFS 2 features	1	16	–

<b>Problem 2 (a)</b>	<b>Bias (V)</b>	<b>MW<sub>2</sub> Error [%]</b>	<b>Limestone Error [%]</b>	<b>Granite Error [%]</b>
	0.4	2.076	29.81	1.91
	0.7	62.62	47.26	17.94
	0.3, 0.4	0.34	12.77	3.82
	0.3-1.2	0.34	17.84	1.43
<b>Problem 2 (b)</b>	<b>Bias (V)</b>	<b>Granite Error [%]</b>	<b>Hornfels Error [%]</b>	-
	0.3	55	46	-
	1.1	0	20	-
	0.6, 0.7	5	27	-
	0.3-1.2	1	17	-
	CCFS 2 features	1	16	-

For the first bias voltage set, the Euclidean-distance classifier consistently shows good classification for all three scenes as shown by the thematic maps in the first column in Fig. 8(a)–(c). This observation is confirmed by the classification errors in Table III for this case. In contrast, for the second bias voltage set the Euclidean-distance classifier cannot discriminate successfully between the filters, metal holders and background, as shown by the thematic maps in the second column in Fig. 8(a)–(c). This result and the classification errors in Table III show that the bias voltage at 0.7 V is not a good choice for these scenes. However, adding a second bias voltage at 0.6 V to the second set (resulting in our third bias voltage set) improves the classification as shown by the thematic maps in third column in Fig. 8(a)–(c). Finally, the thematic maps in the last column in Fig. 8(a)–(c) and the classification errors in Table III indicate almost perfect classification results for the fourth set of bias voltages, i.e., when all ten biases are used.

Thematic maps and classification errors for the rock classification problem are shown in Figs. 8(d) and 9, and Table IV, respectively. For the granite-limestone-MW<sub>2</sub> classification problem, we use four different sets of bias voltages defined as follows: (i) one bias at 0.4 V; (ii) one bias at 0.7 V; (iii) two biases at 0.3 and 0.4 V; and (iv) all ten biases in the range of 0.3–1.2 V. The first and the second thematic maps in Fig. 8(d) show that the first bias voltage set gives more accurate results than the second one, i.e., bias at 0.4 V is more effective for this scene content than the bias at 0.7 V. Using the third bias voltage set, which combines two biases at 0.3 and 0.4 V, improves the classification accuracy compared to the first two cases [the third thematic map in Fig. 8(d)]. Moreover, from the fourth thematic map in Fig. 8(d), we see that the third bias set gives results comparable to those using the fourth bias set, i.e., when all ten DWELL FPA bands are used.

To summarize, the results for the filter and granite-limestone-MW<sub>2</sub> classification problems demonstrate that accurate classification can be achieved by either considering a broader range of spectral information, namely, by using all bias voltages, or by using specific biases, or combination thereof. However, as our results show, the optimal subselection of the bias range depends on the specific classification problem. To reduce this ambiguity, we will use the CCFS algorithm in order to determine the optimal superposition bands for the granite-hornfels classification problem.

The feasibility of the CCFS concept is illustrated by the thematic map shown in Fig. 9(right). This map is obtained using two superposition CCFS bands in conjunction with the Euclidean-distance classifier. The first superposition band is optimized with respect to granite and the second is optimized with respect to hornfels. Recall, that these superposition bands are obtained via optimal superposition weights,  $a_{v_1}, \dots, a_{v_n}$  [11]. Note, that there is one such set of weights for each class; numerical values of these weights are not shown here for brevity. We see that the two superposition bands are sufficient to yield classification results that are essentially the same as those obtained using all ten DWELL FPA bands, as shown in the first and the second thematic maps in Fig. 9, middle

and right, respectively. Moreover, the classification results presented in Table IV indicate that in general, the two CCFS bands give better accuracy than that obtained from two randomly selected bands, as for example the combination of 0.6 and 0.7 V.

In the next section, we investigate in greater details the dependence of the between-class separability and the classification accuracy on the selection of the bias voltages for the granite-limestone-MW2 classification problem.

## B. Separability Analysis and Optimal Bias Selection

The idea of using a measure of between class separability to select spectral bands or features has been widely used in machine learning and computer vision. Let  $\boldsymbol{\mu}_G = (\mu_G(v_1), \dots, \mu_G(v_m))$  and  $\boldsymbol{\mu}_L = (\mu_L(v_1), \dots, \mu_L(v_m))$  denote the means of class granite and limestone, respectively, for given biases  $v_1, \dots, v_m$ .

We define the normalized separability between the two rock types, granite, and limestone, at bias voltage  $v_i$  as follows:

$$S_{v_i} = \frac{|\mu_G(v_i) - \mu_L(v_i)|}{\|\boldsymbol{\mu}_G - \boldsymbol{\mu}_L\|} \quad (5)$$

where  $|\mu_G(v_i) - \mu_L(v_i)|$  is the net difference distance between the means of the classes granite and limestone, respectively, when bias voltage  $v_i$  is applied, and  $\|\boldsymbol{\mu}_G - \boldsymbol{\mu}_L\|$  denotes the Euclidean-distance between the (vector) mean of classes granite and limestone when all biases are used. The normalized separability metric provides information about the contribution of the individual biases to the overall separability achieved when all bias voltages are used.

Fig. 10 (left) shows the normalized separability between the granite and limestone classes from the scene in Fig. 4(d) as a function of the applied bias. For bias voltages 0.3, 0.4, and 0.5 V, the normalized separability between the granite and limestone classes is in the range of 40%–50%. This means that bands at 0.3, 0.4, or 0.5 V contribute almost half of the total separability between the two rocks. At 0.6 V, the normalized separability drops to approximately 18% and it is below 30% at 0.7 V. In the range of 0.9–1.1 V, the individual band's contributions are all below 20%.

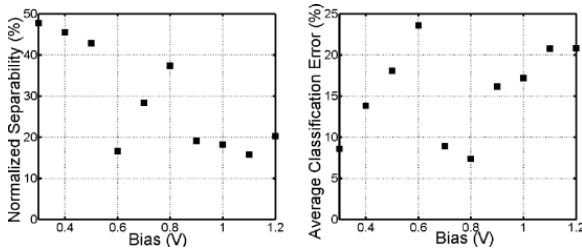


Fig. 10. Left: normalized separability between granite and limestone for each individual bias used. Right: average (over the two classes) classification error between granite and limestone as a function of each individual bias used.

Fig. 10 (right) shows the average classification error between granite and limestone classes as a function of the applied bias. The average classification error is calculated by dividing the number of misclassified pixels between the two classes over the number of tested pixels per class and averaging over the number of classes.

Comparison between the results presented in Fig. 10, left and right, demonstrates that for a given classification problem, bias voltages that exhibit higher contribution to the overall separability in general lead to lower classification errors. For example, in the range of 0.3–0.5 V, for all three biases characterized by high granite-

limestone separability, the averaged classification error is between 8%–18%. The bias voltage of 0.6 V, characterized by the lowest contribution to the overall separability of 18%, leads to highest classification error of 24%. For the bias voltages of 0.7 and 0.8 V, the normalized separability between the two classes increases, which leads to a decrease in the classification errors to 9% and 7% for the 0.7 and 0.8 V biases, respectively. In the range of 0.9–1.2 V, where the bands exhibit relatively low, contribution to the overall separability (20%), the classification error increases and varies between 15%–21%.

Fig. 11 (left) shows the progression in the normalized separability between granite and limestone as bias voltages are added one by one. In reference to the normalized separability calculated as described by (5), let

$$V = \{v_1, \dots, v_n\}$$

denote set of all bias voltages and

$$\alpha = i_1, i_2, \dots, i_k \quad 1 < k \leq 10$$

be a multi-index, where  $1 \leq i_m \leq n$ . We define the subset  $V_\alpha$  of  $V$  as follows:

$$V_\alpha = \{v_{i_1}, \dots, v_{i_k}\}$$

and the progression of the normalized separability as a function of the number of bias voltages can now be recast as

$$S_{V_\alpha} = \frac{\|\mu_G(V_\alpha) - \mu_L(V_\alpha)\|}{\|\mu_G - \mu_L\|}. \quad (6)$$

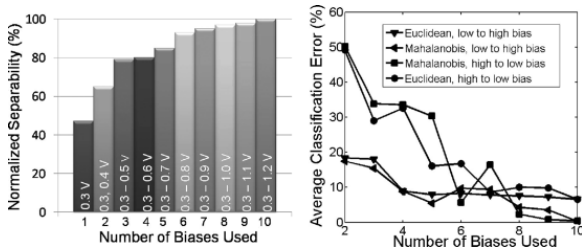


Fig. 11. Left: normalized separability between granite and limestone when bands are added sequentially in an increasing order. Right: average classification error between granite, limestone, and filter when bands are added sequentially in an increasing and a decreasing order.

We observe that the addition of the bias at 0.4 V to the bias at 0.3 V increases the contribution to the total separability (when all biases are used) from 50% to 70%. Furthermore, the addition of the bias at 0.5 V increases the contribution up to 80%. However, note that sequential addition of the biases in the range of 0.6–1.2 V increases the contribution to the total separability only by 20%. This observation is consistent with the results shown in Fig. 10 (left).

Fig. 11 (right) shows the progression of the average classification error for granite, limestone and MW2 for two classifiers (based upon the Euclidean and Mahalanobis distances) as a function of the number of applied biases. Two cases are considered. In the first case, the bands are added in sequential order from low bias to high bias, one at a time. As expected, the highest error (18%) is achieved when only bias 0.3 V and bias 0.4 V are used and the lowest error is achieved when all biases are used. Note, that when all biases are used, the Mahalanobis-distance classifier gives lower error than the Euclidean-distance classifier. In the second case, the biases are added sequentially in descending order, one at a time. As in the first case, the highest error is achieved when



only two bias voltages are used (1.2 and 1.1 V, respectively) and the lowest error is achieved again when all biases are used.

**Table V** Optimal Band Selection Based on Minimizing the Average Classification Error for Mahalanobis-Distance Classifier for the Granite, Limestone, and the MW<sub>2</sub> Classification Problem

Classification Error [%]	Number of Biases	Biases (V)
5.83	2 of 10	0.3, 1.2
1.16	3 of 10	0.8, 0.9, 1.2
0.36	4 of 10	0.6, 0.8, 0.9, 1.2
0.0	5 of 10	0.3, 0.6, 0.8, 0.9, 1.2
0.0	6 of 10	0.3, 0.6, 0.7, 0.8, 0.9, 1.2
0.08	7 of 10	0.3, 0.5, 0.7, 0.8, 0.9, 1.1, 1.2
0.12	8 of 10	0.3, 0.4, 0.5, 0.7, 0.8, 0.9, 1.1, 1.2
0.35	9 of 10	0.3, 0.5, 0.6, 0.7, 0.8, 0.9, 1.0, 1.1, 1.2
0.34	10 of 10	0.3, 0.4, 0.5, 0.6, 0.7, 0.8, 0.9, 1.0, 1.1, 1.2

Classification Error [%]	Number of biases	Biases (V)
5.83	2 fo 10	0.3, 1.2
1.16	3 fo 10	0.8, 0.9, 1.2
0.36	4 fo 10	0.6, 0.8, 0.9, 1.2
0.0	5 fo 10	0.3, 0.6, 0.8, 0.9, 1.2
0.0	6 fo 10	0.3, 0.6, 0.7, 0.8, 0.9, 1.2
0.08	7 fo 10	0.3, 0.5, 0.7, 0.8, 0.9, 1.1, 1.2
0.12	8 fo 10	0.3, 0.4, 0.5, 0.7, 0.8, 0.9, 1.1, 1.2
0.35	9 fo 10	0.3, 0.5, 0.6, 0.7, 0.8, 0.9, 1.0, 1.1, 1.2
0.34	10 fo 10	0.3, 0.4, 0.5, 0.6, 0.7, 0.8, 0.9, 1.0, 1.1, 1.2

**Table VI** Optimal Band Selection Based on Minimizing the Average Classification Error for the Mahalanobis-Distance Classifier for the Granite and Limestone Pair

Classification Error [%]	Number of Biases	Biases (V)
4.14	2 of 10	0.6, 0.9
1.40	3 of 10	0.8, 0.9, 1.2
0.20	4 of 10	0.6, 0.8, 0.9, 1.2
0.0	5 of 10	0.3, 0.6, 0.8, 0.9, 1.2
0.0	6 of 10	0.3, 0.6, 0.7, 0.8, 0.9, 1.2
0.1	7 of 10	0.3, 0.5, 0.7, 0.8, 0.9, 1.1, 1.2
0.0	8 of 10	0.3, 0.4, 0.5, 0.7, 0.8, 0.9, 1.1, 1.2
0.39	9 of 10	0.3, 0.5, 0.6, 0.7, 0.8, 0.9, 1.0, 1.1, 1.2
0.40	10 of 10	0.3, 0.4, 0.5, 0.6, 0.7, 0.8, 0.9, 1.0, 1.1, 1.2

Classification Error [%]	Number of biases	Biases (V)
4.14	2 fo 10	0.6, 0.9
1.4	3 fo 10	0.8, 0.9, 1.2
0.2	4 fo 10	0.6, 0.8, 0.9, 1.2
0.0	5 fo 10	0.3, 0.6, 0.8, 0.9, 1.2
0.0	6 fo 10	0.3, 0.6, 0.7, 0.8, 0.9, 1.2
0.01	7 fo 10	0.3, 0.5, 0.7, 0.8, 0.9, 1.1, 1.2
0.0	8 fo 10	0.3, 0.4, 0.5, 0.7, 0.8, 0.9, 1.1, 1.2
0.39	9 fo 10	0.3, 0.5, 0.6, 0.7, 0.8, 0.9, 1.0, 1.1, 1.2
0.40	10 fo 10	0.3, 0.4, 0.5, 0.6, 0.7, 0.8, 0.9, 1.0, 1.1, 1.2

**Table VII** Optimal Band Selection Based on Minimizing the Average Classification Error for the Mahalanobis-Distance Classifier for the Granite and Hornfels Classification Problem

Classification Error [%]	Number of Biases	Biases (V)
3.98	2 of 10	1.0, 1.2
1.32	3 of 10	0.9, 1.0, 1.1
1.15	4 of 10	0.6, 0.8, 0.9, 1.1
0.98	5 of 10	0.6, 0.7, 0.9, 1.0, 1.2
1.01	6 of 10	0.5, 0.6, 0.7, 0.9, 1.1, 1.2
1.10	7 of 10	0.4, 0.5, 0.6, 0.7, 0.8, 0.9, 1.1
1.09	8 of 10	0.3, 0.4, 0.5, 0.7, 0.8, 0.9, 1.0, 1.1
1.24	9 of 10	0.3, 0.4, 0.5, 0.6, 0.7, 0.8, 0.9, 1.0, 1.1
1.27	10 of 10	0.3, 0.4, 0.5, 0.6, 0.7, 0.8, 0.9, 1.0, 1.1, 1.2

Classification Error [%]	Number of biases	Biases (V)
3.98	2 fo 10	1.0, 1.2
1.32	3 fo 10	0.9, 1.0, 1.1
1.15	4 fo 10	0.6, 0.8, 0.9, 1.1
0.98	5 fo 10	0.6, 0.7, 0.9, 1.0, 1.2
1.01	6 fo 10	0.5, 0.6, 0.7, 0.9, 1.1, 1.2
1.10	7 fo 10	0.4, 0.5, 0.6, 0.7, 0.8, 0.9, 1.1
1.09	8 fo 10	0.3, 0.4, 0.5, 0.7, 0.8, 0.9, 1.1, 1.2
1.24	9 fo 10	0.3, 0.4, 0.5, 0.6, 0.7, 0.8, 0.9, 1.0, 1.1
1.27	10 fo 10	0.3, 0.4, 0.5, 0.6, 0.7, 0.8, 0.9, 1.0, 1.1, 1.2

Notably, the error magnitude depends on the order in which the biases are added. Clearly, two DWELL biases at 1.2 and 1.1 V lead to more than twice the increase in the classification error (~50%) compared to biases at 0.3 and 0.4 V (18%). The trend is similar up to 5–6 biases used for classification.

Tables V–VII present the results of an exhaustive search for selection of optimal combinations of biases, minimizing the average classification error for the Mahalanobis-distance classifier, as a function of number of biases used. Table V presents the results for granite, limestone and the MW<sub>2</sub> filter classification problem. Table VI presents the results for the pair granite and limestone, and Table VII presents the results for granite and hornfels. The overall trend in the results presented in Tables V–VII demonstrates that as the number of biases increases, the classification error decreases. For example, the optimal combination of two bias voltages gives a classification error of approximately 6% for the granite, limestone and the MW<sub>2</sub> filter classification problem, while using nine of ten biases leads to an error of less than 1%. For the granite-limestone pair, the optimal combination of two bias voltages gives a classification error of approximately 4%, while for the optimal combination of nine of ten band the error is again less than 1%. Same observations hold for granite and hornfels as seen from the results presented in Table VII. Note however that in all three cases, optimal combinations of five biases and above give almost the same classification error as the case when all biases are used.

## SECTION V. Conclusion

In this paper, we have demonstrated for the first time the MS-based classification of the DWELL FPA by exploiting the DWELL's bias tunability along with traditional and customized algorithms. The DWELL FPA performance has been validated using two classification problems: 1) separation between three mid IR spectral filters and 2) discrimination among two pairs of rocks and a filter. The second classification problem is more challenging than the first one as the rocks exhibit lower overall spectral contrast within the tuning range of the DWELL FPA.

Our verification studies with the DWELL FPA data allow us to draw several conclusions. First, the studies show that, as a result of its bias tunability, the DWELL FPA can successfully capture spectral contrast between different materials, which, in turn, enables their accurate classification. Second, the results from the separability

and classification analysis for optimal bias selection in both problems demonstrate that accurate classification can be achieved by either considering a broader range of spectral information, i.e., by using all bias voltages, or by using specific biases, or combination thereof. Our results also indicate that the optimal subselection of the bias range depends on the classification problem. As expected, the optimal selection of biases varies from case to case. Finally, a customized feature-selection algorithms that specifically addresses the abundant spectral overlap and noise in the DWELL bands, such as the CCFS, can additionally enhance the MS capability of the DWELL FPA by selecting only few optimized superposition bands that yield the same classification results as when using all DWELL FPA bands.

## ACKNOWLEDGMENT

The authors would like to thank Dr. L. J. Crossey and Dr. V. Atudorei with the Department of Earth and Planetary Sciences, University of New Mexico, for providing rock samples.

## References

1. C. A. Musca, J. Antoszewski, K. J. Winchester, K. K. M. B. D. S. A. J. Keating, T. Nguyen, J. M. Dell, L. Faraone, P. Mitra, J. D. Beck, M. R. Skokan, J. E. Robinson, "Monolithic integration of an infrared photon detector with a MEMS-based tunable filter", *IEEE Electron Device Lett.*, vol. 26, no. 12, pp. 888-890, Dec. 2005.
2. N. Gupta, R. Dahmani, S. Choy, "Acousto-optic tunable filter based visible- to near-infrared spectropolarimetric imager", *Opt. Eng.*, vol. 41, pp. 1033-1038, May 2002.
3. S. Krishna, "Newly-demonstrated 320  $\times$  256 focal plane array uses quantum-dot-based detectors", *Int. Society for Opt. Eng. (SPIE)*, pp. 1-2, 2006.
4. S. D. Gunapala, S. V. Bandara, C. J. Hill, D. Z. Ting, J. K. Liu, S. B. Rafol, E. R. Blazejewski, J. M. Mumolo, S. A. Keo, S. Krishna, Y.-C. Chang, C. A. Shott, "640  $\times$  512 pixels long-wavelength infrared (LWIR) quantum-dot infrared photodetector (QDIP) imaging focal plane array", *IEEE J. Quantum Electron.*, vol. 43, pp. 230-237, 2007.
5. S. Krishna, D. Forman, S. Annamalai, P. Dow, P. Varangis, T. Tumolillo, A. Gray, J. Zilko, K. Sun, M. Liu, J. Campbell, D. Carothers, "Demonstration of a 320 by 256 two-color focal plane array using InAs/InGaAs quantum dots in well detectors", *Appl. Phys. Lett.*, vol. 86, pp. 1935011-1935013, 2005.
6. D. A. B. Miller, D. S. Chemla, T. C. Damen, A. C. Gossard, W. Wiegmann, T. H. Wood, C. A. Burrus, "Band-edge electroabsorption in quantum well structures: The quantum-confined stark effect", *Phys. Rev. Lett.*, vol. 53, pp. 2173-2176, 1984.
7. P. Aivaliotis, N. Vukmirovic, E. A. Zibik, J. W. Cockburn, D. Indjin, P. Harrison, C. Groves, J. P. R. David, M. Hopkinson, L. R. Wilson, "Stark shift of the spectral response in quantum dots-in-a-well infrared photodetectors", *J. Phys. D*, vol. 40, pp. 5537-5540, 2007.
8. . Sakoglu, M. M. Hayat, J. S. Tyo, P. Dowd, S. Annamalai, K. T. Posani, S. Krishna, "Statistical adaptive sensing by detectors with spectrally overlapping bands", *Appl. Opt.*, vol. 45, pp. 7224-7234, 2006.
9. W.-Y. Jang, M. M. Hayat, J. S. Tyo, R. S. Attaluri, T. E. Vandervelde, Y. D. Sharma, R. Sheno, A. Stintz, E. R. Cantwell, S. Bender, S. Krishna, "Demonstration of bias controlled algorithmic tuning of quantum dots in a well mid-infrared detectors", *IEEE J. Quantum Electron.*, vol. 45, pp. 5537-5540, 2009.
10. W.-Y. Jang, M. M. Hayat, S. Bender, Y. D. Sharma, J. Shao, S. Krishna, "Performance enhancement of an algorithmic spectrometer with quantum-dots-in-a-well infrared photodetectors", *Proc. Int. Symp. Spectral Sensing Research (ISSR 08)*, pp. 1, 2008-Jun.-2327.
11. B. S. Paskaleva, M. M. Hayat, Z. Wang, J. S. Tyo, S. Krishna, "Canonical correlation feature selection for sensors with overlapping bands: Theory and application", *IEEE Trans. Geosci. Remote Sens.*, vol. 46, no. 10, pp. 3346-3358, 2008.

12. W.-Y. Jang, B. Paskaleva, M. M. Hayat, S. Krishna, "Spectrally adaptive nanoscale quantum dot sensors" in Handbook of Science and Technology for Homeland Security, New York:Wiley, 2010.
13. S. Krishna, "InAs/InGaAs quantum dots in a well photodetectors", *J. Phys. D: Appl. Phys.*, vol. 38, pp. 2142-2150, 2005.
14. J. Andrews, W.-Y. Jang, J. E. Pezoa, Y. D. Sharma, S. J. Lee, S. K. Noh, M. M. Hayat, S. Restaino, S. W. Teare, S. Krishna, "Demonstration of a bias tunable quantum dots-in-a-well focal plane array", *Infrared Phys. Technol.*, vol. 52, pp. 380-384, Nov. 2009.
15. E. Varley, M. Lenz, S. J. Lee, J. S. Brown, D. A. Ramirez, A. Stintz, S. Krishna, "Single bump two-color quantum dot camera", *Appl. Phys. Lett.*, vol. 91, pp. 081120-1-3, 2007.
16. A. Milton, F. Barone, M. Kruer, "Influence of nonuniformity on infrared focal plane array performance", *Opt. Eng. (Bellingham)*, vol. 24, pp. 855-862, 1985.
17. R. O. Duda, P. E. Hart, D. G. Strok, Pattern Classification, New York:Wiley, 2000.
18. S. Krishna, "The infrared retina", *J. Phys. D: Appl. Phys.*, vol. 42, pp. 1-6, 2009.

## Keywords

### IEEE Keywords

Detectors,

Pixel,

Optical sensors,

Optical imaging,

Materials,

Metals

### INSPEC: Controlled Indexing

focal planes,

image classification,

object detection,

quantum dots

### INSPEC: Non-Controlled Indexing

multispectral image classification,

bias-tunable infrared quantum dots-in-a-well focal plane array,

multispectral image sensing,

spectral response,

bias voltage sequence,

classification algorithm,

IR filter

- **Author Keywords**

Bias tunability,

dots-in-a-well (DWELL),

infrared (IR) detector,

multispectral (MS) classification,

quantum-dots,

rock classification